Dynamics of freely swimming flexible foils

Silas Alben,[1,a)] Charles Witt,[2] T. Vernon Baker,[2]
Erik Anderson,[2] and George V. Lauder[3]

[1]*School of Mathematics, Georgia Institute of Technology, Atlanta, Georgia 30332-0160, USA*
[2]*Department of Mechanical Engineering, Grove City College, Grove City, Pennsylvania 16127, USA*
[3]*Department of Organismic and Evolutionary Biology, Harvard University, Cambridge, Massachusetts 02138, USA*

We use modeling and simulations guided by initial experiments to study thin foils which are oscillated at the leading edge and are free to move unidirectionally under the resulting fluid forces. We find resonant-like peaks in the swimming speed as a function of foil length and rigidity. We find good agreement between the inviscid model and the experiment in the foil motions (particularly the wavelengths of their shapes), the dependences of their swimming speeds on foil length and rigidity, and the corresponding flows. The model predicts that the foil speed is proportional to foil length to the $-1/3$ power and foil rigidity to the $2/15$ power. These scalings give a good collapse of the experimental data. © *2012 American Institute of Physics*. [http://dx.doi.org/10.1063/1.4709477]

I. INTRODUCTION

The study of fish locomotion has been very active for the last several decades, and includes work by groups in biology,[1–5] applied mathematics,[6–9] and engineering.[10,11] Many of these studies consider models of swimming fish—flexible foils or sheets—which oscillate in a steady oncoming flow of a prescribed speed. These studies have greatly improved our understanding of how thrust forces depend on the body shape and motion, particularly in terms of the pattern of vortices generated in the wake.[12,13] Lauder and co-workers have quantified the kinematics of freely swimming fish,[14,15] including particle image velocimetry studies of flow structures around the bodies and fins.

Recent work has considered freely moving models of swimmers[16,17] and fliers.[18–20] A simple passive or oscillating body which is mechanically coupled to the surrounding flow can exhibit a rich variety of dynamical behaviors.[21–25] In Ref. 26 the swimming speed is not set *a priori*, but is instead optimized by varying the swimming motion. Borazjani and Sotiropoulos used simulations to determine Strouhal and Reynolds numbers at which carangiform or anguilliform motions yield higher efficiency in self-propelled swimmers.[27,28] Kern and Koumoutsakos also considered optimal burst velocity in self-propelled anguilliform simulations,[29] and Shirgoankar *et al.* studied gymnotiform locomotion experimentally and computationally.[30]

In this work we study a basic physical model for a swimming body, introduced in Refs. 12, 13, and 16. We perform experiments on thin flexible foils, driven by periodic heaving at the leading edge. The foils are allowed to move freely through the fluid in the swimming direction, and attain a state of steady swimming with a nearly constant speed. We measure foil swimming speed versus foil length and bending rigidity, and we find a resonant-like response, with multiple peaks and troughs in swimming speed. In order to understand this apparent resonant phenomenon discovered in our experimental work, we perform inviscid simulations, which also find multiple peaks and troughs in swimming speed, moving from a peak to a trough when the number of wavelengths on the foil increases by approximately one quarter. We consider approximate solutions in the form of

---

a)Electronic mail: alben@math.gatech.edu.

sinusoidal traveling waves, in the limit of wavy foils (large length and/or small bending rigidity). The approximate solutions allow us to find asymptotic power-law scalings for the dependences of swimming speed on length and bending rigidity. The scalings give a good collapse of the experimental data, even for relatively rigid foils. We also compare the foil shapes and flows with those from the experiment, and find good qualitative and quantitative agreement, considering the simplifying assumptions in the model.

II. FREE FOIL EXPERIMENTS

Experiments on the swimming of flexible self-propelling foils were performed using the computer-controlled robotic flapping foil apparatus described in Refs. 12, 13, and 16 and shown schematically in Figure 1. Briefly, this apparatus uses a carriage containing heave and pitch motors mounted on low-friction airbearing rods above a recirculating flow tank. A linear encoder mounted on the carriage is used to monitor upstream-downstream (x) position, while rotary encoders on the motors provide data on the motion generated. Flexible plastic foils are attached via a stainless steel sting to the motors above, and can be moved in pitch and heave at the leading edge. The experimental results described here were done with a heave motion of $A\cos(2\pi ft)$ at the leading edge of each foil, with amplitude $A = 1.0$ cm and frequency $f = 2.0$ Hz. A LabVIEW control program is used to match the flow tank speed to the swimming speed of the foils, so that true self-propulsion is achieved, with thrust forces balancing drag forces when averaged over a flapping cycle. Self-propulsion was verified in control experiments using an ATI Nano17 six-axis force/torque transducer mounted on the foil shaft to measure foil forces during propulsion. Thrust force coefficients integrated to a value not significantly different from zero over a flapping cycle.[13] Two slightly different versions of the flapping foil robotic device were used to gather data on the self-propelled speed of flexible foils. The first version was used to generate the data shown in Figure 5 of swimming speed versus foil length. A second iteration of this device was used to gather data on the effects of span shown in Table II. Due to modifications to the flapping device, foil swimming speeds are not directly comparable between Table II and Figure 5.
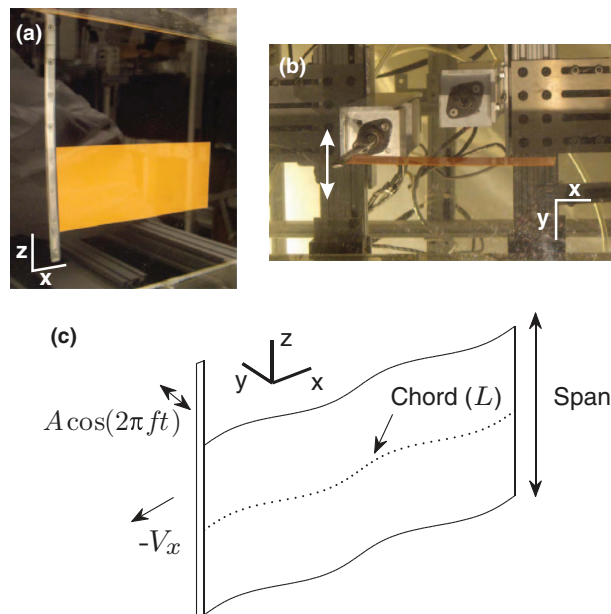

FIG. 1. Foil apparatus shown in side view (a) and bottom view (b). The foil is the orange rectangular plate which is clamped at its leading edge. In (b), the carriage and airbearing rods are visible above the foil. A schematic diagram in side view is shown in (c).

TABLE I. Foil characteristics. In this paper, the foils' spans are 6.8 cm, except where noted (i.e., Table II, Sec. IV).

Foil	Thickness (cm)	EI (dyn cm^2)
A	0.075	3.85×10^6
B	0.052	9.88×10^5
C	0.033	3.22×10^5
D	0.011	3.28×10^4
E	0.004	1.12×10^3

Plastic shim stock materials of varying thickness were used to make flexible foils of different flexural stiffnesses (Table I). In order of decreasing thickness (and decreasing bending modulus), the foil materials are labeled A–E, for convenience. Most experiments were done with rectangular foils having a 6.8 cm span to allow comparison with our previous work,[12,13] but some experiments involved foils of 19 cm span (see Table II, Sec. IV) to estimate the consequences of reducing three-dimensional effects from the foil edges in comparing experimental data to results from the model. We varied foil length to study the effect of changing chord on self-propelled speed and the waveforms achieved during propulsion. Flexural stiffnesses of the foil materials, shown in Table I, were calculated using the Young's moduli of each material measured using an Instron materials testing machine and the dimensions of the foils. The plastics were found to be linearly elastic over a strain range of 0.002–0.16. McHenry *et al.* measured fish flexural stiffness using three-point bending, and reported values for flexural stiffness along the body of pumpkinseed sunfish *Lepomis gibbosus* that range from approximately 10^6 dyn cm^2 near the head to 10^3 dyn cm^2 near the tail.[31] These values fall within the range of foil flexural stiffness of the foils used here. High-speed video of foil swimming was obtained with a Photron camera imaging at 500 Hz. A custom MATLAB program was used to obtain midline images of the foils to produce "snapshot" pictures of the waveforms at various times through the flapping cycle (e.g., Figure 2).

High-speed video was also used to collect time-resolved particle image velocimetry data on foils during self-propulsion using the same approach as in our previous research.[16,32,33] Briefly, a continuous beam Coherent 10 W laser was used to generate a light sheet approximately 20 cm wide that intersected the swimming foils at the midspan position. Flow was seeded with small nearly-neutrally-buoyant particles, and image sequences of the flow were obtained using high-speed video
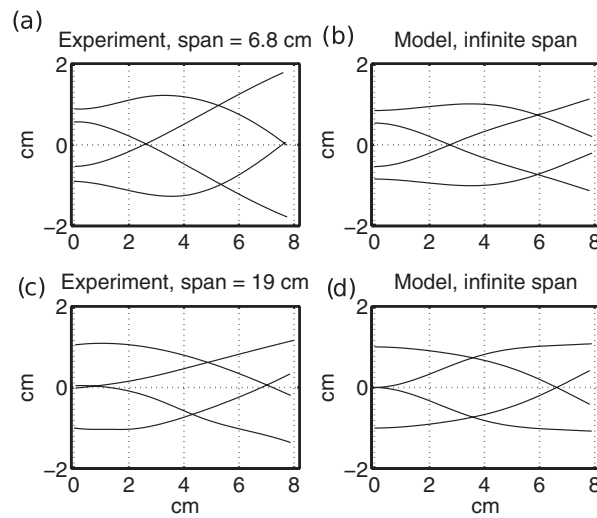

FIG. 2. Comparison of foil shape snapshots in the experiment with spans 6.8 cm (a) and 19 cm (c) with the model (infinite span) at instants (b) corresponding to (a) and (d) corresponding to (c). Data are shown for foil D (see Table I) with chord of 8 cm.

at 500 Hz. Standard cross-correlation analysis using DaVis 7.2 software (Lavision, Inc.) generated a time series of velocity vectors representing flow patterns throughout the flapping cycle. Standard flow characteristics were calculated including vorticity and streamlines to illustrate hydrodynamic flows near the foil and in the near wake (e.g., Figure 8). Due to the shadows cast by the foils, flow structures were only visible on one side of the swimming foil.

III. BODY-VORTEX-SHEET MODEL

We model the freely swimming foil as a one-dimensional body moving in a two-dimensional fluid. The body sheds a vortex sheet into the fluid at its trailing edge. Because the Reynolds number is in the range 10^3–10^5, we may assume the vortex sheet does not diffuse much under fluid viscosity, and remains a one-dimensional curvilinear sheet in the fluid. The model is similar to that in Ref. 34. For small-amplitude body deflections, a linearized version of the model was analyzed in Ref. 35. In these works, the horizontal motion of the body was prescribed and steady, whereas in the present work, the horizontal motion of the body is coupled to the fluid according to Newton's second law. Due to this coupling, the present problem has an additional source of nonlinearity. Viscous boundary layer drag is included in the present model, and is an important component of the force balance in the horizontal direction. Viscous boundary layer drag may be comparable to or even greater than pressure drag for objects which are nearly aligned with the oncoming flow,[36] which is often the case for our foils. We also note that Refs. 34 and 35 mainly considered pitching at the leading edge, while the present work considers only heaving; this difference was considered in Ref. 35 and does not change the qualitative results.

We briefly summarize the parts of the model which are the same as in Refs. 34 and 35 and emphasize the aspects which are new. The foil moves as an inextensible elastica according to the equation

$$R_1 \partial_{tt}\zeta(s,t) = \partial_s(T(s,t)e^{i\theta(s,t)}) - R_2\partial_s(\partial_s\kappa(s,t)ie^{i\theta(s,t)}) - [p](s,t)ie^{i\theta(s,t)}. \tag{1}$$

Here $R_1 = 2\rho_s/\rho_f L$ is the dimensionless body mass and $R_2 = 32EI/\rho_f f^2 L^5$ is the dimensionless bending rigidity. The foil mass per unit length is ρ_s, the fluid mass per unit area is ρ_f, L is the foil length, EI is the foil bending rigidity, and f is the frequency of heaving. The position of the foil in the complex plane is $\zeta(s,t)$, a function of arc length s and time t. The tension in the foil is $T(s,t)$ and the pressure jump across the foil is $[p](s,t)$. The foil's tangent angle is $\theta(s,t)$, $\kappa(s,t) = \partial_s\theta(s,t)$ is the curvature, and $e^{i\theta(s,t)}$ is the unit tangent to the foil. Equation (1) is made dimensionless by nondimensionalizing time by $1/f$, distance by $L/2$, and mass by $\rho_f L^2/4$.

Equation (1) is solved together with the boundary condition that the foil is heaved harmonically in time at the leading edge with (dimensionless) amplitude A and zero tangent angle. In accordance with the experiment, we assume that the foil is held at the leading edge by a clamp which is free to move horizontally. At the trailing edge, the foil experiences zero force and torque. Thus, the boundary conditions are

$$\zeta(-1,t) = x(t) + iA\cos(2\pi t); \quad \theta(-1,t) = 0, \tag{2}$$

$$T(1,t) = \kappa(1,t) = \partial_s\kappa(1,t) = 0. \tag{3}$$

The horizontal position of the clamp $x(t)$ is given by Newton's second law in the horizontal direction

$$(M_{driver} + \rho_s L)\frac{d^2x}{dt^2}(t) = F_{x,fluid}. \tag{4}$$

The driver, i.e., the object which performs the heaving at the clamp, has mass M_{driver}, and the mass of the foil is $\rho_s L$. $F_{x,fluid}$ is the horizontal force exerted by the fluid on the foil and clamp. Nondimensionalizing (4) in the same way as Eq. (1), we obtain

$$(m_{driver} + 2R_1)\frac{d^2x}{dt^2}(t) = F_{x,fluid}. \tag{5}$$

Here $m_{driver} = 4M_{driver}/\rho_f L^2$ and the other quantities in Eq. (5) are dimensionless from now on. In the experiment, $M_{driver} = 8$ kg, and we replace ρ_f by the product of ρ, the fluid mass per unit *volume*, with the span of the foil (typically 6.8 cm). Then m_{driver} ranges from 5 to 200 as L ranges over the chord lengths used in the experiment. Thus, the driver mass is dominant over the fluid inertia in the experiment, and the model results shown for comparison in Sec. IV. When we remove the driver mass from the model in Sec. V, the results for average speed and foil deflection change relatively little, while the fluctuations in horizontal motion increase greatly.

In Eq. (5), $F_{x,\,fluid}$ is the horizontal component of pressure force on the foil plus a term due to viscous skin friction:

$$F_{x,\,fluid} = \int_{-1}^{1} [p](s, t) \sin(\theta(s, t)) ds + F_{x,\,visc}. \tag{6}$$

Here we omit the force due to leading edge suction, because the leading edge vortices do not remain attached to the foil in the experiment. Since the foil is nearly aligned with the oncoming flow, the skin friction may be comparable to the pressure force. We assume that the skin friction is approximately the same as that for a flat plate moving steadily at a speed equal to the instantaneous average horizontal flow speed along the foil, $U(t)$. The viscous stress at position s is then (see Refs. 36 and 37):

$$\tau_{visc}(s, t) = \frac{1}{3} \rho_f \sqrt{\frac{\nu U(t)^3}{s + 1}}. \tag{7}$$

Nondimensionalizing,

$$\tau_{visc}(s, t) = \frac{2}{3} \sqrt{\frac{\nu}{f L^2}} \frac{V_x(t)^{3/2}}{\sqrt{s + 1}}, \tag{8}$$

$$F_{x,\,visc} = 2 \int_{-1}^{1} \tau_{visc}(s, t) ds = \frac{8\sqrt{2}}{3} \sqrt{\frac{\nu}{f L^2}} V_x(t)^{3/2}. \tag{9}$$

Here $V_x = 2U/fL$ and $\sqrt{\nu/fL^2}$ is the inverse square root of a Reynolds number. This Reynolds number is $10^3 - 10^5$ in the experiment. The term $F_{x,\,visc}$ opposes the foil's forward motion, which is in the $-\hat{e}_x$ direction. In our simulations, when we remove skin friction, the speed of a nearly rigid foil may increase by more than 100%, while the speed of a very flexible foil increases by about 10%. Skin friction is used in the simulation results shown subsequently in this paper. The viscous stresses act tangentially to the foil, and tangential gradients in viscous stress are counteracted by the tension which makes the foil inextensible. Thus the viscous stresses do not play an important role in the bending of the foil, described by Eq. (1). We also note that the main effect of gravity is to stretch the foil slightly (by about 0.01%) in the chordwise direction, so inextensibility remains a good approximation in the presence of gravity. We combine Eqs. (5), (6), and (9) to obtain the equation for the horizontal motion of the leading-edge clamp:

$$(m_{driver} + 2R_1) \frac{d^2 x}{dt^2}(t) = \int_{-1}^{1} [p](s, t) \sin(\theta(s, t)) ds + \frac{8\sqrt{2}}{3} \sqrt{\frac{\nu}{f L^2}} \left(\frac{dx}{dt}(t)\right)^{3/2}. \tag{10}$$

The pressure force in Eqs. (1) and (10) is obtained by solving for the inviscid flow around a flexible body which continually sheds a vortex sheet from its trailing edge. The model here is the same as in Ref. 34 and we repeat it briefly for completeness.

The complex conjugate of the flow velocity (u_x, u_y) at any point z in the flow can be calculated in terms of the vortex sheet strength γ by integrating the vorticity in the bound and free sheets against the Biot-Savart kernel:[38]

$$u_x(z) - i u_y(z) = \frac{1}{2\pi i} \int_{C_b + C_f} \frac{\gamma(s', t)}{z - \zeta(s', t)} ds'. \tag{11}$$

Here C_b is the contour representing the foil $(-1 \leq s' \leq 1)$ and C_f is the contour representing the free vortex sheet $(1 < s' \leq s_{max})$. We can express the average w of the flow velocities on the two sides of

any point $\zeta(s, t)$ on C_b or C_f by taking the average of the limits of Eq. (11) as z approaches $\zeta(s, t)$ from above and below the contours:

$$\bar{w}(s, t) = \frac{1}{2\pi i} P \int_{-1}^{1} \frac{\gamma(s', t)}{\zeta(s, t) - \zeta(s', t)} ds' + b(s, t), \tag{12}$$

$$b(s, t) = \frac{1}{2\pi i} \int_{1}^{s_{\max}} \frac{\gamma(s', t)}{\zeta(s, t) - \zeta(s', t)} ds'. \tag{13}$$

In Eq. (12), $\bar{w}$ is the complex conjugate of w, and the integral is of principal-value type.

We can rewrite $b(s, t)$ in a more convenient Lagrangian form. The free vortex sheet consists of a line of fluid particles which are continually advected away from the trailing end of the foil, for $t \geq 0$. There is a bound vortex sheet with strength $\gamma(s, t)$ along the foil, and we also use γ for $s > 1$, to describe the strength of the shed vortex sheet. The circulation is the integral of γ:

$$\Gamma(s, t) = \int_{s_{\max}}^{s} \gamma(s', t) ds', \quad -1 < s < s_{\max}, \tag{14}$$

and the total circulation in the free sheet is $\Gamma_+(t) = \int_{s_{\max}}^{1} \gamma \, ds'$. According to the Helmholtz laws for vorticity conservation in two-dimensional flows, specialized to a vortex sheet, $\Gamma(s, t)$ is conserved on particles which move with the fluid (Ref. 38, p. 30). Thus each fluid particle in C_f carries the value of circulation $\Gamma(s, t) = \Gamma(1, t^*)$ it has at the time t^* when it is emitted from the trailing edge of the foil. We can label material points by Γ, and reparametrize b in Eq. (13) by circulation Γ using $\gamma \, ds = d\Gamma$:

$$b(s, t) = -\frac{1}{2\pi i} \int_{0}^{\Gamma_+(t)} \frac{d\Gamma'}{\zeta(s, t) - \zeta(\Gamma', t)}. \tag{15}$$

On the free vortex sheet C_f, it can be shown that material points $\zeta(\Gamma, t)$ move with velocity w (Ref. 38, p. 31). This gives the Birkhoff-Rott equation for the evolution of the free vortex sheet,

$$\frac{\partial \bar{\zeta}}{\partial t}(\Gamma, t) = \frac{1}{2\pi i} \fint_{C_b} \frac{\gamma(s', t)}{\zeta(\Gamma, t) - \zeta(s', t)} ds' + \frac{1}{2\pi i} \int_{C_f} \frac{d\Gamma'}{\zeta(\Gamma, t) - \zeta(\Gamma', t)}, \quad \zeta(\Gamma, t) \in C_f. \tag{16}$$

Using Γ to label points on the free sheet eliminates the need for a separate evolution equation for $\gamma(s, t)$ on the free sheet. This is an important advantage of using the Lagrangian description of the free sheet.

We apply Eq. (12) to $\zeta(s, t)$ on the foil, to express the kinematic condition that fluid does not penetrate the foil on either side. In other words, the component of the foil velocity normal to the foil equals the same component of w:

$$\text{Im}\left(e^{-i\theta(s,t)} \partial_t \zeta(s, t)\right) = \text{Im}\left(e^{-i\theta(s,t)} w(s, t)\right), \qquad \zeta(s, t) \in C_b, \tag{17}$$

$$\text{Im}\left(e^{-i\theta(s,t)} \partial_t \zeta(s, t)\right) = \text{Im}\left(e^{-i\theta(s,t)} \left(\frac{1}{2\pi i} \fint_{-1}^{1} \frac{\gamma(s', t) ds'}{\zeta(s) - \zeta(s')} + b(s, t)\right)\right), \quad \zeta(s, t) \in C_b. \tag{18}$$

When the left hand side of Eq. (18) and $b(s, t)$ are known, the general solution $\gamma(s, t)$ has inverse-square-root singularities at $s = \pm 1$ (Ref. 39). If we define $v(s, t)$, the bounded part of $\gamma(s, t)$, by

$$\gamma(s, t) = \frac{v(s, t)}{\sqrt{1 - s^2}}, \tag{19}$$

the kinematic condition becomes

$$\text{Im}\left(e^{-i\theta(s,t)} \partial_t \zeta(s, t)\right) = \text{Im}\left(e^{-i\theta(s,t)} \left(\frac{1}{2\pi i} P \int_{-1}^{1} \frac{v(s', t) ds'}{\sqrt{1 - s'^2}(\zeta(s) - \zeta(s'))}\right) + b(s, t)\right),$$

$$\zeta(s, t) \in C_b. \tag{20}$$

A complication arises in using Eq. (16) to solve for the dynamics of a free vortex sheet numerically. The equation is ill-posed, which causes numerical errors to increase rapidly.[40] Krasny and others showed that the ill-posedness can be removed by modifying the singular kernel in Eq. (16) using a smoothing parameter δ.[41] The δ-smoothed versions of Eqs. (16) and (20) are

$$\partial_t \bar{\zeta}(s,t) = \frac{1}{2\pi i} P \int_{-1}^{1} \frac{\gamma(s',t)ds'}{\zeta(s,t) - \zeta(s',t)} + b_\delta(s,t), \qquad \zeta(s,t) \in C_f, \tag{21}$$

$$\text{Im}\left(e^{-i\theta(s,t)} \partial_t \zeta(s,t)\right) = \text{Im}\left(e^{-i\theta(s,t)} \left(\frac{1}{2\pi i} P\int_{-1}^{1} \frac{v(s',t)ds'}{\sqrt{1-s'^2}(\zeta(s)-\zeta(s'))}\right) + b_\delta(s,t)\right), \ \zeta(s,t) \in C_b, \tag{22}$$

respectively, where

$$b_\delta(s,t) = -\frac{1}{2\pi i} P \int_{0}^{\Gamma_+(t)} d\Lambda' \frac{\overline{\zeta(s,t) - \zeta(\Lambda',t)}}{|\zeta(s,t) - \zeta(\Lambda',t)|^2 + \delta^2}. \tag{23}$$

In the Appendix we show that the foil speed does not change much as δ is decreased from 0.2 to 0.1. In this work we mainly use $\delta = 0.2$. The instantaneous total circulation in the free sheet, $\Gamma_+(t)$, is determined by the Kutta condition, which states that at each time t the fluid velocity at the trailing edge $s = 1$ is finite. In particular, γ, which is also the tangential component of the jump in fluid velocity across the foil, must be finite at the trailing edge. Using Eq. (19), the Kutta condition becomes

$$v(1,t) = 0. \tag{24}$$

At each time t, Eq. (24) is a constraint which we use, together with the conservation of circulation in the flow, to determine $\Gamma_+(t)$ as described in Ref. 34.

One can relate the pressure jump across the foil $[p]$ to the vortex sheet strength along the foil by a version of the unsteady Bernoulli equation. One writes the Euler equations for fluid velocities at points above and below the foil, and takes the limit that the points approach each other from opposite sides of the foil (see Ref. 38, p. 31, and Ref. 42). The difference of these equations is an evolution equation for the difference of the fluid velocities, which is $\gamma \hat{s}$ (the normal component is zero by the no-penetration condition on either side of the foil). The evolution equation for the vortex sheet strength γ is[42]

$$\gamma_t + \partial_s((\mu - \tau)\gamma) = \partial_s[p], \tag{25}$$

where $\tau(s,t)$ is the tangential component of the fin velocity and $\mu(s,t)$ is the tangential component of the average fluid velocity:

$$\tau(s,t) = \text{Re}\left(\partial_t \zeta(s,t)e^{-i\theta(s,t)}\right); \quad \mu(s,t) = \text{Re}\left(w(s,t)e^{-i\theta(s,t)}\right). \tag{26}$$

The pressure jump across the free sheet is zero, which yields the boundary condition for Eq. (25),

$$[p]\,|_{s=1} = 0. \tag{27}$$

We integrate Eq. (25) along C_b to determine $[p](s,t)$ on the foil, $-1 \leq s \leq 1$.

IV. NUMERICAL RESULTS AND COMPARISON

We begin by simulating foils over the range of parameters used in the experiment, and compare the shapes and speeds of the foils. The numerical method and studies of convergence with respect to spatial and temporal discretizations are given in Ref. 34. While the aspect ratio (span divided by chord) ranges from 0.2 to 2 in the experiment, it is infinite in the model. In Figure 2, we compare snapshots over one period of flapping for foil D, with a chord length of 8 cm. Panel (a) shows four snapshots from the experiment with span 6.8 cm, while panel (b) shows four snapshots from the simulation at the same instants as in panel (a). The deflections are noticeably larger in panel (a).
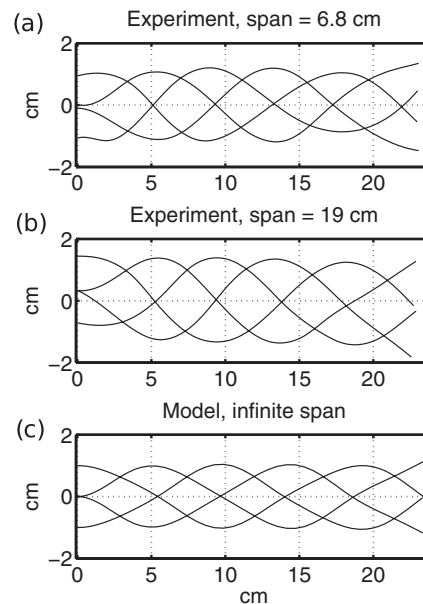
FIG. 3. Comparison of foil shape snapshots in the experiment with spans 6.8 cm (a) and 19 cm (b) with the model (infinite span) at corresponding phases 0, $\pi/2$, π, and $3\pi/2$ (c). Data are shown for foil D (see Table I) with chord of 24 cm.

Panel (c) shows snapshots for a foil from the experiment which has the same chord as in panel a, but with a span of 19 cm, nearly three times larger. Since the model corresponds to infinite span, we expect better agreement with this case, and panel (d) shows the model foil at the four instants shown in panel (c) (different from panels (a) and (b)). The deflection agrees better now, though the tangent angles are smaller near the trailing edge in the simulation.

Figure 3 shows a similar comparison but for foils of chord length 24 cm. Snapshots from the experiment with different spans are given in panels (a) and (b), and since the instants in panels (a) and (b) are nearly the same now, we compare both with just a single sequence of snapshots from the model, in panel (c). There are more wavelengths on the foil because it is longer (more on this shortly), and all three plots agree well in the deflection magnitudes and the number of wavelengths on the foil. Again, the deflection is smaller in the model than in the experiment.

Figure 4 shows a similar comparison for foil A, the stiffest. For both the chord lengths of 8 cm (a)–(c) and 24 cm (d)–(f), we find a similar number of wavelengths among the model and experimental foils. At 24 cm, the model shape has a shorter wavelength, with a smaller overall deflection.

In Figures 2–4, one reason for the smaller deflection in the model may be its increased span. Intuitively, when the span is much less than the chord, fluid is more likely to flow spanwise along and around the foil. The pressure difference across the foil may thus be reduced, but it is unclear whether the foil deflection should be increased or decreased as a consequence. The fluid pressure may increase or decrease foil deflection at different instants during the heaving cycle. In Figures 2(a) and 2(c), the foil with smaller span undergoes larger deflection, while in Figures 4(d) and 4(e), the foil with larger span undergoes larger deflection, so the relationship between span and foil deflection is not monotonic, and probably not simple. However, the magnitude of the variations in experimental results with span show that span effects can account for the discrepancy in shapes between the model (with infinite span) and the experiment. The discrepancy in shapes is not large in any case.

We note that span effects have been studied in the context of a different problem, the flag flutter instability. A model by Eloy *et al.*[43] has found that flags with smaller ratio of span to chord remain stable up to larger oncoming flow speeds.

Table II shows the effect of span on swimming speed for our experiment. We find that for both the more flexible (D) and stiffer (A) foils, larger span leads to a large increase in swimming speed. The increase is about 20% for foil D and much larger—from 80% to 90%—for foil A, which is
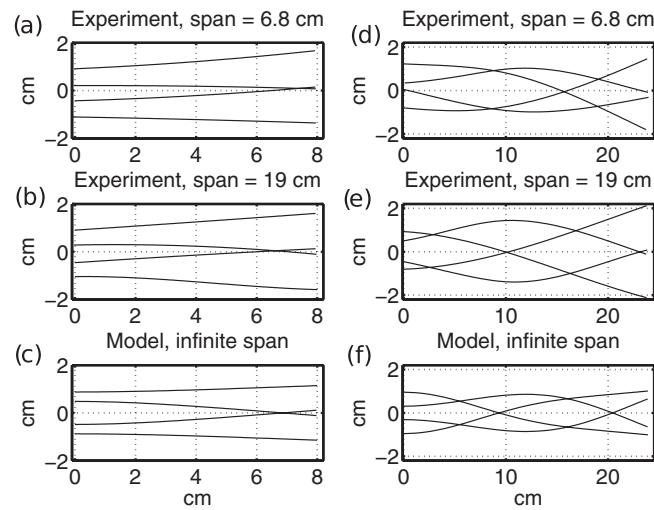
FIG. 4. Comparison of foil shape snapshots in the experiment and model for foil A (see Table I). Panels (a)–(c) have chord length 8 cm and correspond to the experiment with spans 6.8 cm (a) and 19 cm (b), and the model (infinite span) (c) at phases 0.08*2π, 0.33*2π, 0.58*2π, and 0.83*2π, respectively. Panels (d)–(f) have chord length 24 cm and correspond to the experiment with spans 6.8 cm (d) and 19 cm (e), and the model (infinite span) (f) at phases 0.24*2π, 0.49*2π, 0.74*2π, and 0.99*2π, respectively.

much stiffer. For a larger span, the flow is more closely two-dimensional over most of the foil. In this case, the flow along the span is smaller, so more of the fluid momentum is in the downstream, or chordwise direction. Hence, it is reasonable that the foil travels faster with a larger span. We also note that the increase in speed is much larger for the stiffer foil A, which transmits the force from the driving shaft to the fluid more directly.

In Figure 5 we compare the time-averaged horizontal speeds in the model and experiment, for four different plastics and various lengths. In panels (a)–(c), we find two interior peaks in the experimental data (solid line with error bars), and a series of peaks in the model data (dashed line with dots). The spacing between the peaks is similar for the experiment and the model, though the locations of the peaks are shifted. One source of discrepancy is again the difference in span (6.8 cm for the experiment, infinite for the model). In the experimental data of Table II, the foils with larger span had speeds which were larger by 20%–90%. Thus it makes sense that the peak speeds for the model should be significantly higher than those for the experiment (which they are, by about 30%–90%, depending on L and EI). The model does not have some of the sources of friction or damping in the experiment, which is another reason for speeds to be higher in the model. Interestingly, the

TABLE II. Effect of span on swimming speed. The range of speed values are the 95% confidence intervals for the mean foil speeds. Values from three to seven separate trials are used to calculate each of the intervals. The experimental apparatus used to collect these data on the effects of span was not identical to that used for the experimental data shown in Figure 5, and swimming speeds from the two data sets are not comparable.

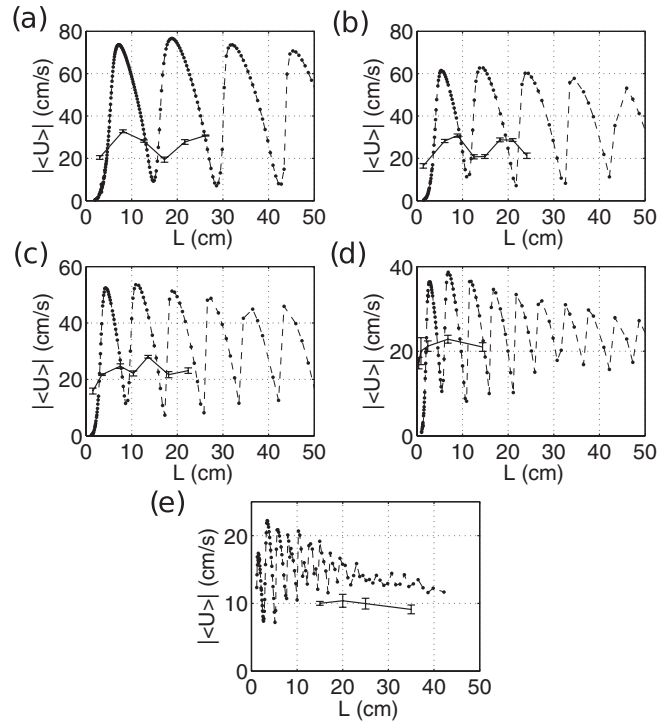| Foil	chord (cm)	Span (cm)	Speed (cm/s)
D	8	6.8	21.2 ± 0.8
D	8	19	25.1 ± 0.6
D	24	6.8	18.9 ± 0.6
D	24	19	23.0 ± 0.4
A	8	6.8	26.5 ± 0.6
A	8	19	50.3 ± 0.3
A	24	6.8	28.0 ± 0.1
A	24	19	51.4 ± 0.3

FIG. 5. Comparison of average swimming speeds in the experiment (solid line) with span 6.8 cm and in the model (dashed line with dots), with infinite span, for the foils of different lengths and five different thicknesses (see Table I). The error bars on the experimental data points show the bounds of the 95% confidence interval. Values from three to seven separate trials are used to calculate each of the error bars. (a)–(e) correspond to foils A–E, respectively. Experimental data plotted here are not comparable to those of Table II, which were obtained with a different experimental setup.

model also has troughs at which the speed is lower than that in the experiment, so the model speed graphs show a much larger amplitude than the experiment from peak to trough.

For the experiment, the peak-to-trough amplitude decreases and the curves are flatter as the bending rigidity decreases, moving from panel (a) to panel (e). A similar trend holds for the model also, though this is in part because the peaks and troughs are not fully resolved in panels (d) and (e), where they are more closely spaced. These variations in the amplitude and spacing between the peaks as *EI* varies will be explained by our analysis in Sec. V C.

We now conduct another shape comparison, this one for the most flexible foils in our study, labeled E in Table I, with velocity data given in Figure 5(e). These foils are much more flexible than the other foils used in this study. In Figure 6 we compare shapes for foil E with chord lengths of 15 cm and 25 cm. We find a larger deflection in the experiment than in the model, consistent with the results of Figures 2 and 3, and the idea that an oscillating foil of smaller span meets less resistance in the fluid, and can thus attain a larger deflection. The experimental foil at 15 cm has a larger deflection and a higher wavenumber than the model foil at 15 cm, with about 1.25 wavelengths on the experimental foil and one wavelength on the model foil at each instant. At 25 cm, the model foil has a larger trailing edge deflection, while the experimental foil has a larger deflection closer to the leading edge. The experimental foil has about 2.4 wavelengths at each instant, while the model foil has about 1.75 wavelengths.

In general, the greater discrepancy between model and experiment for the very flexible foils of Figure 6 versus that for the stiffer foils of Figures 2 and 3 may be attributed to the fact that the very flexible foil may be more sensitive to the differences in the flows, such as complex flow structures along the body and at the trailing edge, and secondary separation of vorticity. By contrast, the motion of stiffer foils may be more strongly controlled by the driving at the leading edge, which is the same for the model and experiment.
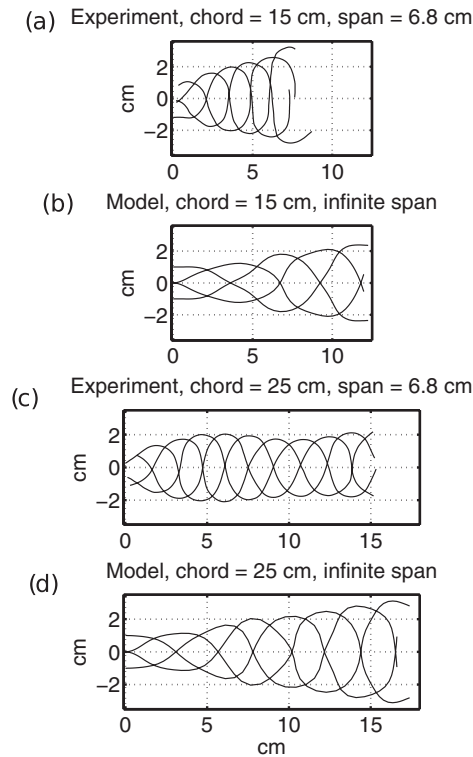
FIG. 6. Comparison of foil shape snapshots in the experiment with span 6.8 cm and chords 15 cm (a) and 25 cm (c) with the model (infinite span) at chords (b) corresponding to (a) and (d) corresponding to (c). Data are shown for foil E (see Table I).

We compare a third instance of foil E, the longest (chord length = 35 cm), in Figure 7. The experimental snapshots, in "a," show peaks in amplitude near the leading edge and the mid-chord, with smaller amplitude at the trailing edge. The model dynamics are much less steady than in Figure 6, so we present three typical sequences of model snapshots in panels (b)–(d), over single heaving periods which are successively 10 periods apart in time. During period 77, the snapshots are asymmetric about the line of zero deflection. By contrast, the model foils in Figure 6 are almost perfectly symmetric about this line. The asymmetry in the longer foil is greater still in Figures 7(c) and 7(d), and apparently results from an instability that sets in for foils which exceed a certain length between 25 and 35 cm. The experimental foil snapshots in panel (a) have about 4.2 wavelengths, while the model snapshots in "b" have about 2.75 wavelengths, and an average deflection which is about 60% larger.

To conclude this comparison section, we give some examples of the flows around foil B in the experiment and model. In Figure 8 we give streamlines for the flow field around the foil in the experiment (panels a, c, and e) and model (b, d, and f). In each panel the foil is shown in light gray (yellow online), the streamlines are white, and for the model (b, d, and f), the vortex sheet is shown in dark gray (blue online). The small particles used to measure the flow speed are barely visible against the black background in panels (a), (c), and (e). The foil shades the flow region above the foil in (a, c, e), in which the flow is not visualized. In (a, c, e) the oncoming flow is subtracted, so in all cases the flow is viewed in a frame in which the foil is moving leftward into quiescent fluid. Panels (a) and (b) show the flows for foils with chord lengths at the first peaks (at lowest L) in foil speed given in Figure 5(b), which occur at $L = 9$ cm for the experiment (Figure 8(a)) and at $L = 5.3$ cm for the model (Figure 8(b)). Panels (c) and (d) show the flows at L corresponding to the first troughs for the experiment and model, and panels (e) and (f) show the flows at the second peaks, respectively.

In the first two experimental frames (a and c), strong vortices can be seen adjacent to the leading edges. These vortices have just been shed from the leading edges as the foil moves upwards. In panel
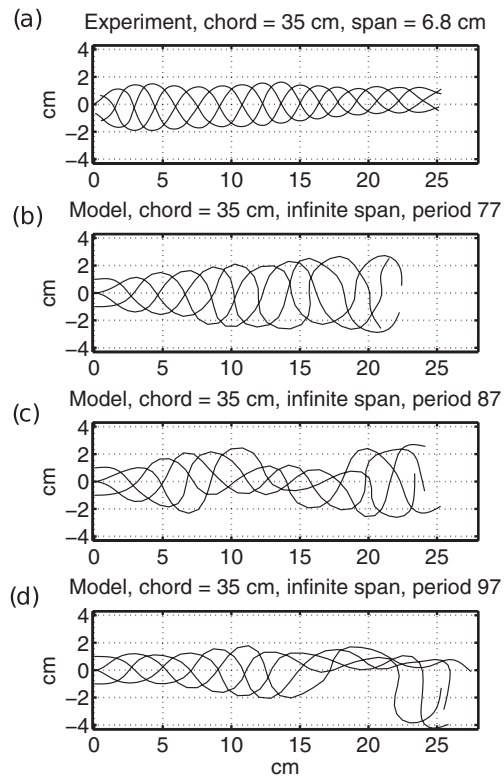
FIG. 7. Comparison of foil shape snapshots in the experiment with span 6.8 cm and chord 35 cm (a) with the model (infinite span) at the same chord and during periods 77 (b), 87 (c), and 97 (d) after start-up. Data are shown for foil E (see Table I).
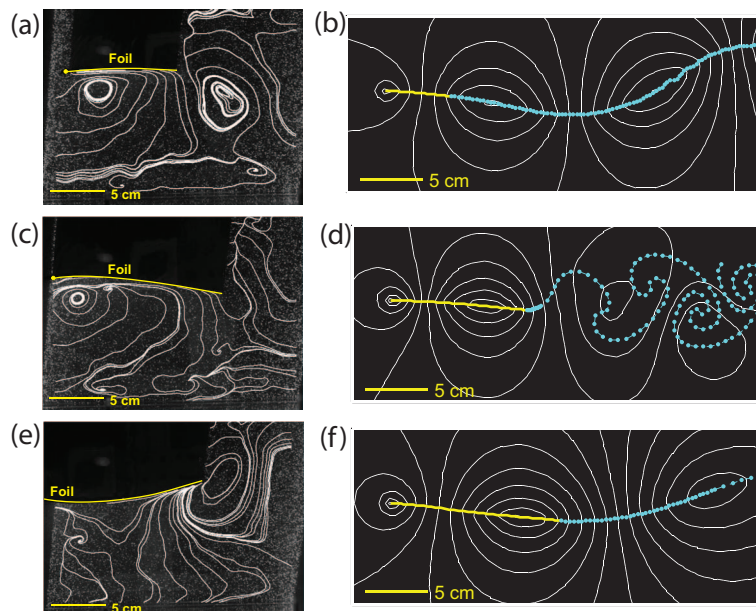

FIG. 8. Comparison of streamlines for the foil B in the experiment (a, c, e) and model (b, d, f). Streamlines are shown at an instant when the foil clamp is midway between its extremes in heaving position, and moving upward, in each of the frames. The foil chord length is 9 cm in (a) and 5.3 cm in (b), which correspond to the first peaks in velocity (at lowest *L*) in Figure 5(b) for the experiment (a) and model (b), respectively. The chord lengths are 15 cm in (c) and 10.9 cm in (d), corresponding to the first troughs in Figure 5(b), and 20 cm in (e) and 13.7 cm in (f), corresponding to the second peaks in Figure 5(b).

(e), the leading one-third of the foil extends out of the frame on the left side, so the leading edge vortex, though present in the flow, is not shown. By contrast, in the model the leading edge vortex is required to be attached to the leading edge at all times (with a singular flow velocity there). It is not yet possible to model the shedding of the leading edge vortex within the model. Because the leading edge vortex does not remain attached in general in the experiment, we have chosen to omit the leading suction force in the model due to the attached leading edge vortex.

In general, the experimental streamlines show much more fine detail than those in the model, which are much smoother. The reason for this is that all of the model vorticity is confined to the foil and the curvilinear vortex sheet, and elsewhere the flow is a potential flow, which is relatively smooth. In the experiment, the strongest vorticity is also concentrated near the foil and wake, though small amounts of vorticity are present elsewhere in the flow. Also, we can see the boundary layer in the experiment as a region adjacent to the foil where the streamlines are parallel to it. In the model, the boundary layer has zero thickness, so the streamlines are not parallel to the foil at the foil surface.

At the trailing edges, for both the experiment and model, we can see a clear difference between the flows at the peaks and the trough. In the experiment at the peaks (a and e), there are strong vortices being shed at the trailing edges. In the experiment at the trough (c), the trailing edge vortex is much weaker. In the model, the vorticity is also much stronger at the velocity peaks (b and f), and much weaker at the trough (d). Upon first inspection, it may be surprising that the vorticity is weaker in panel (d) than in panel (b) or (f), because the vortex sheet is much more rolled up, which is often a signature of stronger vorticity. In panel (d), however, the vortex sheet is more rolled up because the foil is moving much more slowly in (d) than in (b) and (f). Thus, the portion of vortex sheet shown in panel (d) has existed for much longer (about 10 times longer) than in (b) and (f), and has thus had more time to roll up. In panel (d), the streamlines in the foil wake indicate a weaker flow through the wake, similarly to panel (c) in the experiment. In panel (d), the wake consists of weaker, more closely spaced vortices of opposite sign, leading to a weaker net flow through the wake. By contrast, the streamlines between the vortices in panels (b) and (f) indicate a much stronger flow in the wake.

In this section, we have shown that although the model flow is a 2D approximation of the experimental flow, the model and experiment show essentially the same phenomena. As the foil length increases or bending rigidity decreases, the number of wavelengths present on the foil increases. There is also a series of peaks and troughs in swimming speeds, corresponding to the resonances which occur at a discrete series of foil lengths, and a corresponding series of shapes with increasing numbers of wavelengths.

V. ANALYSIS

A. Fixed length and amplitude, varying rigidity

We now present time-dependent foil simulations with fixed length and amplitude, and varying dimensionless bending rigidity R_2 in Eq. (1). While length is the natural control parameter in the experiment, the bending rigidity is a simpler control parameter for the model. The reason is that varying the length changes the dimensionless rigidity as well as the amplitude-to-chord ratio, so the geometry changes as well as the control parameters. After using R_2 as the control parameter, we will redo the analyses with the length as the control parameter.

We fix the ratio of heaving amplitude to foil length at 1/36, sufficiently small to be representative of the long-foil limit. In an important difference from the experiment, in this section we intentionally set to zero the driver mass in Eq. (10), which is large in the experiment. We take the foil mass per unit length to be that of foil D, giving $R_1 = 0.001$. By removing the experimental driver mass in this section we can study a case which is more typical of free swimming in water. Here the body inertia is insignificant relative to the fluid inertia.

As R_2 is decreased below 10^3, we find an alternating sequence of peaks and troughs in average swimming speed, similar to the sequence of peaks and troughs as length is varied in Figure 5. In Figure 9(a), we show foil and flow snapshots at three peaks alternating with three troughs. At the peaks, the vortex sheet wake is quasi-periodic in time, and the corresponding plot of velocity versus time shows a single dominant frequency, which is the heaving frequency. At the troughs, the foil
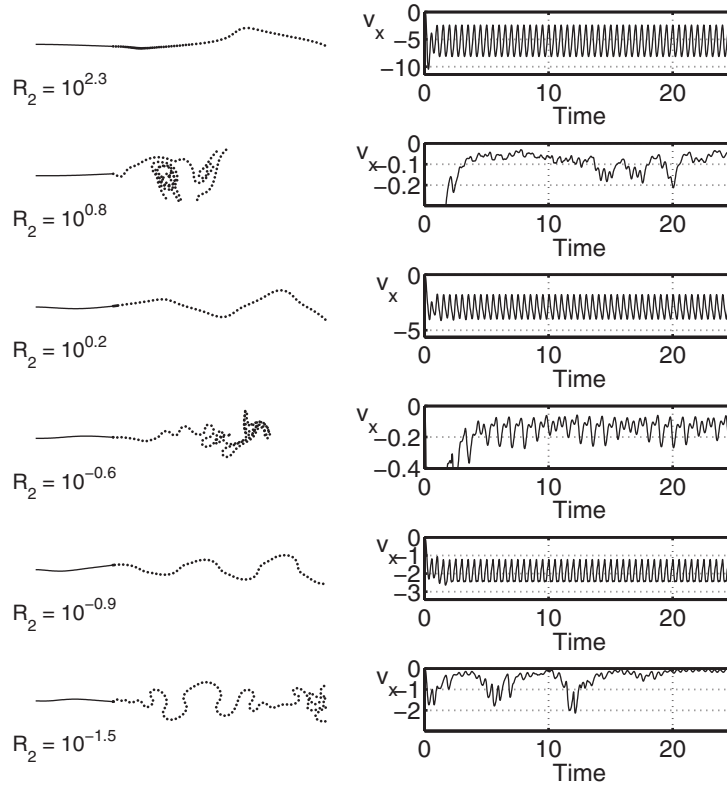
FIG. 9. Results of time-dependent foil simulations with fixed geometry and varying rigidity. (a) Foil and wake snapshots at $t = 17.2$ for different values of R_2. (b) Horizontal velocity versus time corresponding to the snapshots in (a).

wakes are very irregular, and the foils move at much lower average speeds and with smaller trailing edge amplitudes. The corresponding velocity plots show other frequencies superimposed on the heaving frequency. Occasional sudden accelerations and decelerations are typical for $R_2 = 10^{0.8}$ and $10^{-1.5}$. A dominant frequency which is smaller than the heaving frequency can be seen for $R_2 = 10^{-0.6}$. These irregular dynamics are not seen when the driver mass is included, because its large inertia has the effect of averaging the foil acceleration over fluctuations in horizontal thrust.

We plot the average swimming speeds and other key quantities in Figure 10. In panel (a), the swimming speeds for the trajectories of Figure 9 are highlighted with boxes (peaks) and diamonds (troughs). In panel (b), we plot the values of R_2 at which the peaks occur versus their ordinal number k, starting with the largest R_2 at $k = 1$ (or $\log_{10}k = 0$). We find a good fit to the line $R_2 \sim k^{-11/2}$, with another line $R_2 \sim k^{-5}$, for which the fit is less good, shown for comparison. Panel (c) shows the average amplitude of the leading edge curvature for the shapes, which scales as the wavenumber squared for shapes which are approximately sinusoidal. Panel (d) shows the average amplitude of the circulation (or integrated vorticity) in the wake. All four panels show power law behaviors, and we plot power law fitting lines which result from asymptotic arguments we give next.

B. Time-harmonic model

To understand the power-law behaviors in Figure 10, it is helpful to consider a simplified case in which the dynamics occur with a single frequency, the heaving frequency. This occurs when we replace the time-dependent horizontal velocity of the foil with its time-average. This approximately holds in the experiment, because the driver mass is sufficiently large that fluctuations in horizontal foil velocity are very small. We furthermore assume that the amplitude of vertical deflection is small,
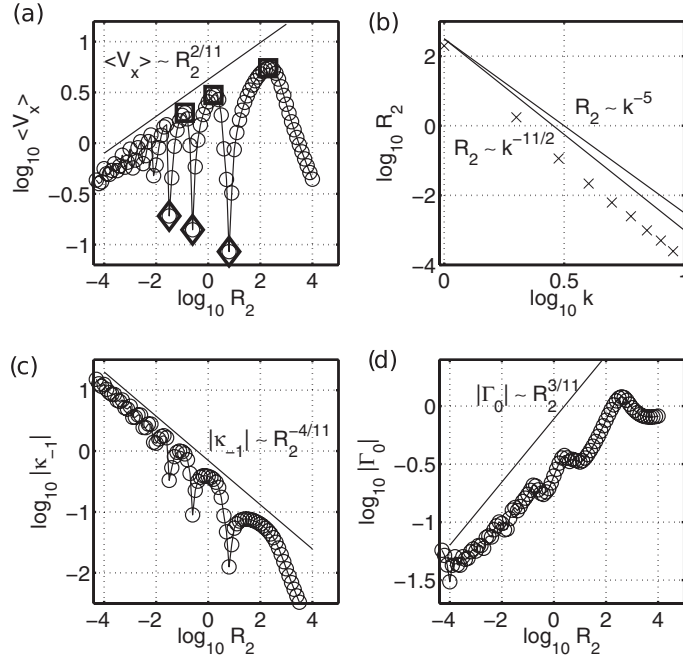
FIG. 10. Results of time-dependent foil simulations versus dimensionless rigidity R_2. (a) Average swimming speed versus R_2. Squares and diamonds correspond to simulations shown in Figure 9. (b) R_2 of peaks from (a) versus ordinal number. (c) Amplitude of leading-edge curvature versus R_2. (d) Amplitude of circulation versus R_2.

which linearizes the equations. Thus, we have

$$y(x,t) = \mathrm{Re}\left(Y(x)e^{i2\pi t}\right); \quad \gamma(x,t) = \mathrm{Re}\left(G(x)e^{i2\pi t}\right),$$

$$[p](x,t) = \mathrm{Re}\left(P(x)e^{i2\pi t}\right); \quad \Gamma_+(t) = \mathrm{Re}\left(\Gamma_0 e^{i2\pi t}\right). \tag{28}$$

When the horizontal speed of the foil is constant, Eqs. (1), (18), and (25) admit solutions with only a single frequency. We showed in Ref. 35 that in the small deflection limit, Eqs. (1), (18), and (25) become

$$0 = -R_2 \partial_x^4 Y - P, \tag{29}$$

$$2\pi i Y + V_x \partial_x Y = \frac{1}{2\pi} \int_{-1}^{1} \frac{G(x')dx'}{x - x'} - \frac{\Gamma_0}{V_x} \int_{1}^{\infty} \frac{e^{-2\pi i(x'-1)/V_x}}{x - x'} dx', \tag{30}$$

$$2\pi i G + V_x \partial_x G = \partial_x P, \tag{31}$$

where V_x is the average horizontal flow velocity relative to the foil, or the negative of the horizontal velocity of the foil moving through a fluid at rest at infinity. Hence, $V_x \geq 0$. We consider the limit in which R_2 is small, so that the foil bends with a high wavenumber k. In this case we may use the estimate given in Ref. 44 to simplify the first integral in Eq. (30) to a Hilbert transform. Using the definition of the exponential integral with an imaginary argument Ei(ix) and its asymptotic behavior for large x,

$$\int_{-1}^{1} \frac{e^{ikx'}dx'}{x - x'} = e^{ikx}\left[i\pi\,\mathrm{sign}(k) + \mathrm{Ei}(-ik(1+x)) - \mathrm{Ei}(ik(1-x))\right], \quad -1 < x < 1, \tag{32}$$

$$\sim e^{ikx}\left[-i\pi\,\mathrm{sign}(k)\right] + O\left(\frac{1}{k}\right) = \mathcal{H}\left(e^{ikx}\right) + O\left(\frac{1}{k}\right), \quad k \gg 1, \ 1 \pm x \gg \frac{1}{k}. \tag{33}$$

Equation (33) shows that the integral on $[-1, 1]$ behaves the same as does the Hilbert transform (denoted $\mathcal{H}$ in Eq. (33)) on $[-\infty, \infty]$ for large k, away from small end regions. Outside of the end regions, we may approximate the solution in the simple form

$$Y(x) = Y_0 e^{ikx}; \quad G(x) = G_0 e^{ikx}; \quad P(x) = P_0 e^{ikx}, \tag{34}$$

where Y_0 is the dimensionless heaving amplitude ($Y_0 = A/L$). We also showed in Ref. 35 that as $k \to \infty$, the last integral in Eq. (30), representing the integral of vorticity over the wake, is subdominant to the other terms. Hence we drop the wake integral. We are thus approximating the foil as an infinite periodic sheet. Even though the approximation is asymptotically valid only for many wavelengths on the foil (k large), we shall see that it gives results which are also a good approximation to those of the fully nonlinear, unsteady model for small numbers of wavelengths (even a fraction of a wavelength) on the foil, which is also more representative of swimming fish bodies and fins.

With these approximations, we can combine Eqs. (29)–(31) into a single equation for Y:

$$0 = -R_2 \partial_x^5 Y + 2(2\pi i + V_x \partial_x)\mathcal{H}(2\pi i Y + V_x \partial_x Y). \tag{35}$$

We now insert the sinusoidal approximation to Y using Eq. (34), and evaluate the Hilbert transform using (33). We obtain

$$R_2 k^5 \sim 2(2\pi + V_x k)^2 \pi \, \text{sign}(k). \tag{36}$$

This equation relates V_x, k, and R_2. The second equation which relates V_x, k, and R_2 is the time-average of Eq. (10), which is

$$0 = \frac{1}{2} \int_{-1}^{1} \text{Re} \left(\bar{P} \partial_x Y \right) dx + \frac{8\sqrt{2}}{3} \sqrt{\frac{\nu}{fL^2}} V_x^{3/2}. \tag{37}$$

Substituting for P from Eq. (29), we can rewrite the integrand in the first term on the right of Eq. (37) as a derivative of the curvature squared. We obtain

$$\frac{1}{2} \int_{-1}^{1} \text{Re} \left(\bar{P} \partial_x Y \right) dx = -\frac{1}{4} R_2 |\partial_{xx} Y|^2 |_{-1}. \tag{38}$$

We have used the condition that the curvature vanishes at the free end, $x = 1$.

The solution $Y(x)$ is well approximated by Eq. (34) away from small (length $\sim 1/k$) regions near the endpoints, where the approximation (33) breaks down. Also, the clamp-free boundary conditions are not obeyed by Eq. (34). Near the endpoints, the slope of the outer sinusoidal solution is $\partial_x Y = O(k)$. At the endpoint, the slope of the inner solution is zero. Thus the slope changes by $O(k)$ over a distance $\sim 1/k$. Hence, the curvature of the inner solution near the clamped end is $O(k^2)$, which is the same order as the outer solution curvature. Thus,

$$-\frac{1}{4} R_2 |\partial_{xx} Y|^2 |_{-1} \sim R_2 Y_0^2 k^4 \sim V_x^{3/2}, \tag{39}$$

using Eq. (37). We eliminate V_x from Eq. (36),

$$V_x \sim R_2^{2/3} k^{8/3} \rightarrow R_2 k^5 \sim 2(2\pi + R_2^{2/3} k^{11/3})^2 \pi. \tag{40}$$

When the quadratic term in Eq. (40) is expanded, there are four terms in the asymptotic relationship. We consider the possible scaling between R_2 and k when k is large by taking the four terms pairwise (yielding six pairs), and checking to see whether the resulting relationship between R_2 and k indeed makes the neglected terms subdominant for large k. Below we list each candidate dominant balance, followed by the scalings of the remaining terms (and whether they are consistent with the terms being subdominant),

$$R_2 k^5 \sim 1 \rightarrow R_2^{2/3} k^{11/3} \sim k^{1/3} \qquad \text{(not consistent)}, \tag{41}$$

$$R_2^{2/3} k^{11/3} \sim 1 \rightarrow R_2 k^5 \sim k^{-1/2}, (R_2^{2/3} k^{11/3})^2 \sim 1 \qquad \text{(consistent)}, \tag{42}$$

$$R_2 k^5 \sim R_2^{2/3} k^{11/3} \rightarrow (R_2^{2/3} k^{11/3})^2 \sim k^2 \gg R_2^{2/3} k^{11/3} \qquad \text{(not consistent)}, \qquad (43)$$

$$R_2 k^5 \sim (R_2^{2/3} k^{11/3})^2 \rightarrow R_2 k^5 \sim k^7 \ll 1 \qquad \text{(not consistent)}, \qquad (44)$$

$$(R_2^{2/3} k^{11/3})^2 \sim 1 \qquad \text{same as (42)}, \qquad (45)$$

$$(R_2^{2/3} k^{11/3})^2 \sim R_2^{2/3} k^{11/3} \qquad \text{same as (42)}. \qquad (46)$$

Equation (42) is the only consistent dominant balance, and it gives $R_2 \sim k^{-11/2}$. In Figure 10(b) we have given the values of R_2 at which the first nine peaks occur in Figure 10(a). Each peak corresponds to a shape approximated by Eq. (34) with $k = \pi/4, 3\pi/4, 5\pi/4, \ldots, 17\pi/4$. The values of R_2 in Figure 10(b) are well approximated as $R_2 \sim k^{-11/2}$, better than the nearby but inconsistent fit $R_2 \sim k^{-5}$ of Eq. (41).

We use Eq. (40) to solve for V_x:

$$R_2 \sim k^{-11/2} \rightarrow V_x \sim R_2^{2/11} \qquad (47)$$

which agrees well with the scaling of the peak velocities in Figure 10(a), even for the peaks at largest R_2, corresponding to less than one wavelength on the foil, shown in Figure 9.

We also check that the leading edge curvature is consistent

$$\kappa|_{-1} \sim \partial_{xx} Y|_{-1} \sim k^2 \sim R_2^{-4/11}, \qquad (48)$$

and find good agreement with Figure 10(c). In Refs. 35 and 44 we derived an expression for the amplitude of the total circulation in the free sheet:

$$\Gamma_0 = \frac{-2 \int_{-1}^{1} (2\pi i Y(x) + V_x \partial_x Y(x)) \sqrt{\frac{1+x}{1-x}} dx}{1 + \frac{2\pi i}{V_x}(1 + \log(2)) + 2\frac{i}{V_x} \int_{-1}^{1} [E_0(x) + \log(1-x)] \sqrt{\frac{1+x}{1-x}} dx}, \qquad (49)$$

$$E_0(x) = -\int_{1}^{\infty} \frac{e^{-2\pi i(x'-1)/V_x}}{x - x'} dx'. \qquad (50)$$

We have found previously that $V_x \sim k^{-1}$ for large k. In the numerator, $Y = Y_0 e^{ikx}$ and $V_x \partial_x Y$ then also has an $O(1)$ magnitude. In Ref. 44 we showed that for $2\pi i Y + V_x \partial_x Y \sim e^{ikx}$, the numerator of Eq. (49) scales as $k^{-1/2}$. In the denominator of Eq. (49), the integral is $O(1)$ as $V_x \sim k^{-1} \rightarrow 0$, so the denominator scales as $1/V_x \sim k$. Thus,

$$|\Gamma_0| \sim \frac{k^{-1/2}}{k} = k^{-3/2} \sim R_2^{3/11}. \qquad (51)$$

We find good agreement with this behavior in Figure 10(d). The complexity of the expression (49) for Γ_0 may require solutions at smaller R_2 than we can simulate to verify the scaling for Γ_0 more clearly.

In order to validate the existence of the time-harmonic solution (28) and quantify its behavior directly, we now solve the time-harmonic equations (29)–(31) and (37) numerically, thus discarding the spatially sinusoidal approximation in Eq. (34). The equations are nonlinear (as V_x appears nonlinearly in Eqs. (30) and (37)), dependent on x and independent of time, with a free vortex sheet wake that is advected horizontally downstream with a sinusoidal distribution of vorticity. Since we do not need to simulate the dynamics of the vortex wake, these simulations (similar to those of Ref. 35) are much less expensive than the fully unsteady simulations we have already shown. Rather than an initial condition, we now use an initial guess for each solution, consisting of zero for all unknowns, except V_x. We vary the initial guess for V_x over 20 logarithmically spaced values from 10^{-5} to 10^2 and record all iterations which converge (satisfy the discretized equations with error
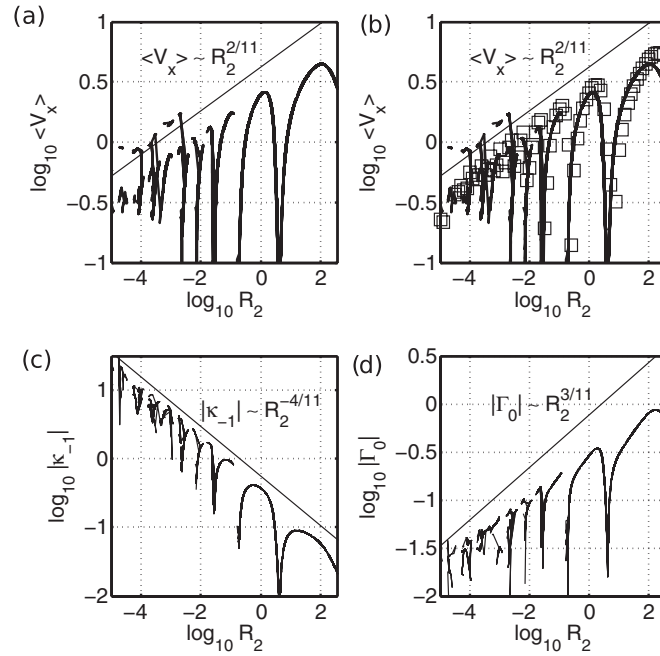
FIG. 11. Results of *time-harmonic* foil solutions with fixed geometry and $A = 10^{-1.25} = 0.056$. (a) Average swimming speed versus R_2. (b) Comparison of average swimming speed in time harmonic model with that of unsteady model (squares), from Figure 10(a). (c) Amplitude of leading-edge curvature versus R_2. (d) Amplitude of circulation versus R_2.

$\leq 10^{-12}$ in 2-norm). The values of V_x, $|\kappa|_{-1}$, and $|\Gamma_0|$ for the converged solutions are plotted in Figure 11. We again find a series of peaks and troughs, similar to the unsteady results of Figure 10. Over most of the range of rigidity, we find only a single solution. However, at smaller values of R_2, additional solutions with larger V_x are found, and are seen in all the panels of Figure 11 for $R_2 < 10^{-2.5}$. We have not investigated the stability of these additional solutions, though it seems likely that they are unstable, since simulations of the unsteady problem at a given R_2 with different initial conditions have found only one average horizontal speed. In Figure 11(b), we plot the unsteady data from Figure 10(a) in squares on top of the time-harmonic data from Figure 11(a). For most of the range of R_2 where the comparison is given, the unsteady data are close to the time-harmonic curves, with slight deviations in the locations of the peaks. We note that perfect agreement is not expected, because many of the unsteady solutions have multiple significant frequencies, not represented by the time-harmonic solutions. However, in Figures 11(a)–11(d) we find very good agreement between the power-law fit lines (with scalings already explained), and the time-harmonic data.

The results of Figure 11 are for a single heaving amplitude of $10^{-1.25}$, or amplitude-to-length ratio $10^{-1.25}/2 \approx 1/36$. In Figure 12 we plot the same results for eight amplitudes ranging over a factor of about five in magnitude. The curves shift upwards as amplitude increases, but the overall scalings are essentially the same. For these amplitudes, the amplitude-to-length ratio is bounded above by $1/9$, so the results may be considered typical for the limit of small amplitude-to-length ratio.

C. Varying length

We have so far considered foils of fixed geometry (length and amplitude), and used the dimensionless rigidity R_2 as the main control parameter. We now return to the experiment, for which length is the main control parameter. We fix the bending rigidity to be that of foil C (see Table I), and allow the length to vary. We perform simulations without the driver mass, with only the foil mass, so the horizontal speed of the foil can fluctuate greatly over one cycle.
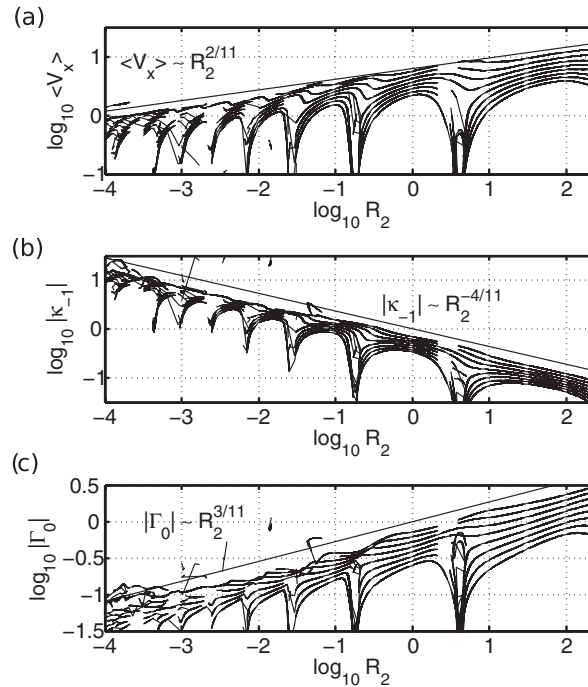
FIG. 12. Results of time-harmonic foil simulations with fixed geometry and eight values of *A/L* ranging from 0.045 to 0.22: $\log_{10}A/L = -1.35, -1.25, -1.15, -1.05, -0.95, -0.85, -0.75, -0.65$. (a) Average swimming speed versus R_2. (b) Amplitude of leading-edge curvature versus R_2. (c) Amplitude of circulation versus R_2.

    In Figure 13(a), we give the average horizontal speed versus foil length. We find a series of peaks and troughs, results which are very similar to those of Figure 5 (in which panel c corresponds to foil C). The only difference in the present simulations is the absence of the driver mass. Also, a logarithmic scale is used on the plots. In Figure 13(b), we give the leading edge curvature, which shows a similar series of peaks and troughs. In Figure 13(c), we plot the *L*-values of the eight peaks in "a" at lowest *L* versus the ordinal number of the peak, which is proportional to the wavenumber *k* of the approximate sinusoidal solution. The approximate power-law fitting lines are explained by the subsequent analysis. First, we show snapshots of the foil and wake corresponding to the peaks and troughs of velocity.
    In Figure 14, we give snapshots of the foils and wakes at a particular instant ($t = 17.2$, chosen arbitrarily), for fourteen lengths with data shown in Figure 13. The lengths are the locations of the first eight peaks (squares) and six troughs (diamonds) of the leading edge curvature shown in Figure 13(b). We have sorted the snapshots so that those for the eight peaks are shown at the top, and those for the six troughs are shown at the bottom. Among the peaks and among the troughs, the values of *L* increase from top to bottom. For the eight peaks, we find that the maxima and minima of deflection are nearly aligned, as shown by the vertical dashed lines. Thus at peaks in velocity, longer foils execute approximately the same motions as shorter foils. The motion is nearly sinusoidal, well approximated by *Y* in Eq. (34). The vortex wake near the foil's trailing edge is approximately an extension of the sinusoidal foil shape.
    The six snapshots at the velocity troughs show much smaller deflections, and a less orderly wake, as expected. However, the wakes are more orderly than those at the velocity troughs when R_2 is varied, shown in Figure 9. The velocities at the troughs in R_2 were generally smaller, while here there is a more consistent forward motion. The wakes are more compressed and rolled-up than at the eight snapshots for the peaks in horizontal velocity, because the foil has not advanced much, so regions of positive and negative vorticity are closer, and the portion of wakes near the foil have existed for longer and have thus had more time to roll up than those in the top eight snapshots.
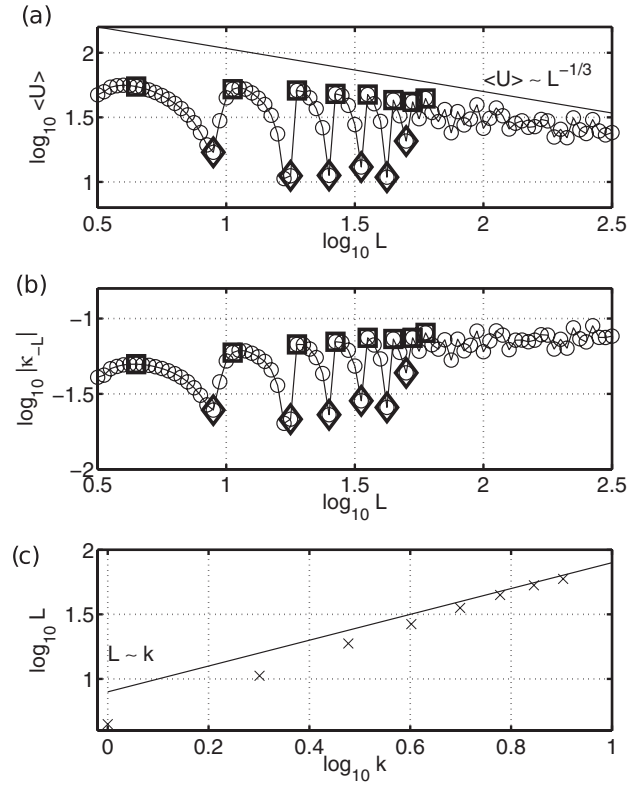
FIG. 13. Results of time-dependent foil simulations with fixed *rigidity* and varying *length*. (a) Average swimming speed versus *L*. Squares and diamonds correspond to simulations shown in Figure 14. (b) Amplitude of leading-edge curvature versus *L*. (c) *L* of peaks from (a) versus ordinal number.

To understand how the horizontal speed and other quantities should scale with L, we repeat the asymptotic analysis of Sec. V B, but now with L as the control parameter instead of R_2. We define two quantities with dimensions of length which are fixed as L varies

$$L_1 = \frac{(8EI)^{1/5}}{f^{2/5}\rho_f^{1/5}} = R_2^{1/5}L, \tag{52}$$

$$L_2 = \sqrt{\frac{\nu}{f}}, \tag{53}$$

and we substitute for Y_0 in Eqs. (28) and (39) its expression as a dimensionless amplitude

$$Y_0 = \frac{2A}{L}. \tag{54}$$

In Sec. V B, A and L were fixed and R_2 varied. Now A and R_2 are fixed and L varies, but the dimensionless equations are the same. Equations (36) and (39) can be written (including the L-dependent coefficient of $V_x^{3/2}$ from Eq. (37)) as

$$\frac{L_1^5}{L^5}k^5 \sim 2(2\pi + V_x k)^2 \pi \, \text{sign}(k), \tag{55}$$

$$\frac{L_1^5}{L^5}\left(\frac{A}{L}\right)^2 k^4 \sim \frac{L_2}{L} V_x^{3/2}. \tag{56}$$
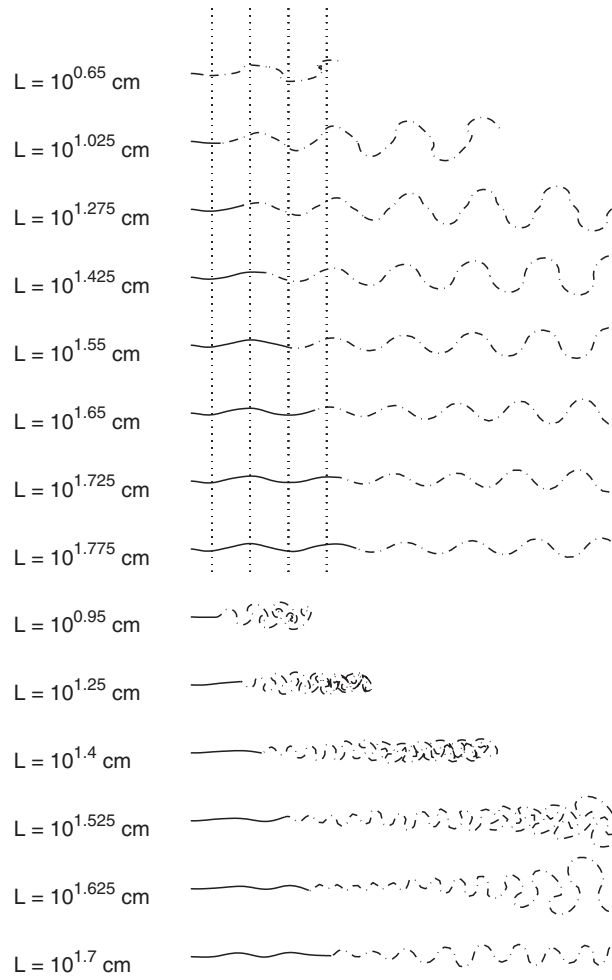
FIG. 14. Results of time-dependent foil simulations with fixed *rigidity* and varying *length*. Shown are foil (solid lines) and wake (dashed-dotted lines) snapshots at $t = 17.2$ for different values of L, given at left, corresponding to the peaks (squares) and troughs (diamonds) in Figures 13(a) and 13(b).

We eliminate V_x using Eq. (56),

$$V_x \sim L^{-4}k^{8/3} \rightarrow L^{-5}k^5 \sim 2(2\pi + L^{-4}k^{11/3})^2\pi. \tag{57}$$

As previously when R_2 was the control parameter, we check six possible dominant balances

$$L^{-5}k^5 \sim 1 \rightarrow L^{-4}k^{11/3} \sim k^{-1/3} \qquad \text{(consistent),} \tag{58}$$

$$L^{-4}k^{11/3} \sim 1 \rightarrow L^{-5}k^5 \sim k^{5/12} \qquad \text{(not consistent),} \tag{59}$$

$$L^{-5}k^5 \sim L^{-4}k^{11/3} \rightarrow (L^{-5}k^5) \sim k^{-5/3} \ll 1 \qquad \text{(not consistent),} \tag{60}$$

$$L^{-5}k^5 \sim (L^{-4}k^{11/3})^2 \rightarrow L \sim k^{7/9}$$
$$L^{-4}k^{11/3} \sim k^{5/9} \ll k^{10/9} \sim L^{-5}k^5 \qquad \text{(consistent),} \tag{61}$$

$$(L^{-4}k^{11/3})^2 \sim 1 \qquad \text{same as (59),} \tag{62}$$

$$(L^{-4}k^{11/3})^2 \sim L^{-4}k^{11/3} \qquad\qquad\qquad \text{same as (59).} \qquad (63)$$

Now there are two consistent dominant balances, (58) and (61). Equation (58) implies that

$$L \sim k; \quad V_x \sim L^{-4/3}; \quad U = LfV_x/2 \sim L^{-1/3}; \kappa|_{-1} \sim L^{-1}k^2 \sim L; \kappa|_{-L/2} = \frac{2}{L}\kappa|_{-1} \sim 1. \quad (64)$$

Here U is the dimensional horizontal speed, and $\kappa|_{-L/2}$ is the dimensional leading edge curvature. Equation (61) implies that

$$L \sim k^{7/9}; \quad V_x \sim L^{-4/7}; \quad U = LfV_x \sim L^{3/7}; \kappa|_{-1} \sim L^{-1}k^2 \sim L^{11/7}; \kappa|_{-L/2} = \frac{2}{L}\kappa|_{-1} \sim L^{4/7}. \quad (65)$$

The scaling (64) states that U decreases with L, while Eq. (65) states that U increases with L. Figure 14(a) shows that U decreases with L, and the fit line corresponding to Eq. (64) gives good agreement there for large L. Similarly, Figure 14(b) shows that the leading edge curvature is nearly flat at large L, and panel (c) shows that the first eight peaks of $\langle U \rangle$ are well-fit by $L \sim k$. Overall, the scalings of Eq. (64) are a much better fit to the numerical data.

The scaling (64) states that $U \sim L^{-1/3}$, which agrees well with the slow decay of velocity in Figures 5 and 13. The experiment also considers the dependence of results on bending rigidity. In Figure 5, the spacing between the peaks decreases with decreasing bending rigidity. Because EI and L are independent parameters, we can include the prefactor involving EI in the dominant balance (64):

$$\frac{L_1^5}{L^5}k^5 \sim 1 \rightarrow k \sim L(EI)^{-1/5}. \qquad (66)$$

The spacing between the peaks in Figure 5 is proportional to the change in L per change in wavenumber, or

$$\frac{\Delta L}{\Delta k} \sim (EI)^{1/5}. \qquad (67)$$

The scaling agrees with the observation of decreasing spacing with decreasing EI. Since EI for the five foils are approximately in the ratio 3600:900:300:30:1, the spacings between the peaks in Figures 5(a)–5(e) should be in the ratio

$$3600^{1/5} : 900^{1/5} : 300^{1/5} : 30^{1/5} : 1^{1/5} = 5.1 : 3.9 : 3.1 : 2.0 : 1 \approx 5 : 4 : 3 : 2 : 1. \qquad (68)$$

This is a good estimate of the relative spacings between the peaks among the five panels of Figure 5. We can determine the dependence of horizontal velocity on EI from Eq. (56), inserting k in terms of EI from Eq. (66):

$$U = LfV_x/2 \sim (EI)^{2/3}L^{-3}k^{8/3} \sim (EI)^{2/15}L^{-1/3}. \qquad (69)$$

The magnitudes of the velocities in the four panels of Figure 5 should thus be in the ratio:

$$3600^{2/15} : 900^{2/15} : 300^{2/15} : 30^{2/15} : 1^{2/15} = 3.0 : 2.5 : 2.1 : 1.6 : 1. \qquad (70)$$

This provides a good estimate of the relative magnitudes of U in Figure 5. To be more precise, we replot the experimental data from Figure 5 with U rescaled by the powers of EI and L in Eq. (69). Figure 15(a) shows the experimental data from each panel of Figure 5 in colors corresponding to the plastic used. Figures 15(b) and 15(c) show the same data with U rescaled by Eq. (69) and L rescaled by Eq. (66). This rescaling of L is appropriate because it aligns the dimensionless foil solutions at a given wavenumber k, and thus also aligns the peaks and troughs in foil velocity, which are determined by k. Figure 15(b) shows the data for four of five foils, and the peaks and troughs of three of these (A, B, C) are closely aligned, considering the approximations which went into deriving the scaling relationships, and the fact that the foils have only zero to two wavelengths for the data shown here. Foil D has the least number of data points, which may not be enough to resolve its peaks and troughs as fully as for the other three foils in panel (b). However, the foil D data lie close to the data for the other foils. Panel (c) shows the same data as in panel (b) plus the data for foil E, with
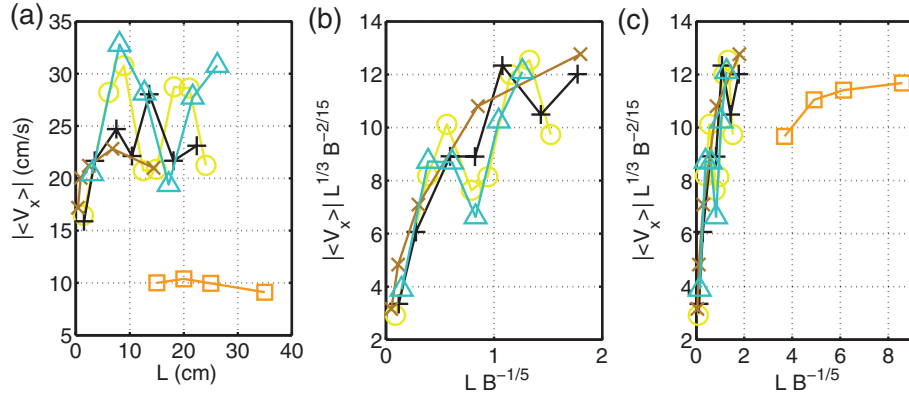
FIG. 15. Rescaling of experimental speed data by factors of length and bending rigidity which correspond to the asymptotic scalings given in Eq. (69). The plot symbols correspond to the foil used (see Table I). Foil A: open triangles (blue), Foil B: open circles (yellow), Foil C: plus signs (black), Foil D: crosses (tan), and Foil E: open squares (orange).

the horizontal axis expanded. The theory predicts that the rescaled velocities should level off as the foils become wavier, and the data for foil E indicates a leveling off at larger $L(EI)^{-1/5}$. Because foil E is much more flexible than the others, the data might have been expected to deviate more from the theory, as occurred in the shape comparisons of Figures 6 and 7.

VI. DISCUSSION AND CONCLUSIONS

We have presented a theoretical and experimental study of the performance of freely swimming flexible foils. Although the model uses a 2D flow while 3D effects are likely to be significant in the experiment, many aspects of the foils—the number of wavelengths in their shapes, their swimming speeds, and the surrounding flows—are captured closely by the model. The model allows for a simple analysis based on sinusoidal solutions that predicts power law scalings for the foil velocities, leading edge curvatures and shed circulation, as well as the distributions of peaks and troughs in these quantities as length and rigidity are varied. The analysis agrees well with the numerical simulations and the experiment in these relationships.

In the Introduction we noted that the peak and troughs seem to indicate a resonant-like response similar to that analyzed in Ref. 35. The main difference between that work and this one is that there the foil was oscillated in a fluid stream with fixed velocity, while here the foil is free to move horizontally. In the earlier work the foil rigidity and speed of the foil relative to the flow were two independent control parameters, while here the speed is a function of the other control parameter (rigidity or length). In the earlier work, resonances occurred at certain values of the rigidity, because the sum of the bending force and fluid inertia vanish at certain values of rigidity, and cannot balance the force due to the leading edge driving unless their amplitude diverges (in the linearized problem). The terms involving the foil speed parameter served to damp the resonances; in the limit that the foil speed tended to zero, the resonances were undamped.

The present work can be considered as a modification of this framework. The foil speed is now a nonlinear function of the foil curvature. We can construct the speed versus R_2 plot from Figure 10(a) by taking data points from the plots of Ref. 35 at various fixed velocities. The locations of the resonances in R_2 are the same. At the peaks of the resonances, there is a finite amount of damping set by solving a nonlinear equation for the foil's horizontal speed. Since the foil speed is a superlinear function of the foil curvature, at the troughs in Figure 10(a), where the foil curvature is small, the speed is very small, so the effect of the damping is negligible, and very steep troughs are seen in Figure 10(a). We conclude that the foil behavior is described by damped resonances, where the amount of damping grows nonlinearly with the response.

Future work may examine further the relationships between the flows in the theory and experiment, and the effects of other parameters held fixed here such as the heaving amplitude and
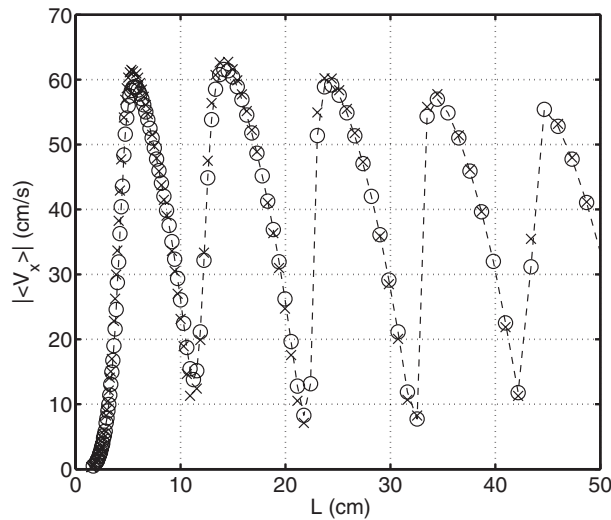
FIG. 16. Comparison of average swimming speeds in the model for two different values of the numerical smoothing parameter δ, 0.1 (circles), and 0.2 (crosses), for the foil B. The data given by the crosses is that in Figure 5(b), also shown in crosses there.

the rectangular foil shape. A study which elaborates on the effects of varying the foil span is also important. We may further consider more complex body actuations such as that described in Ref. 45.

ACKNOWLEDGMENTS

APPENDIX: COMPARISON OF VELOCITIES AT TWO VALUES OF SMOOTHING PARAMETER

In Figure 16 we compare the foil swimming speeds for two different values of δ, 0.1 (circles), and 0.2 (crosses). In general the agreement is very good. The leftmost peak in speed for $\delta = 0.1$ is 4.2% lower than that for $\delta = 0.2$. The other peaks are within 2.5%.

[1] R. Bainbridge, "The speed of swimming of fish as related to size and to the frequency and amplitude of the tail beat," J. Exp. Biol. **35**, 109–133 (1958).

[2] R. W. Blake, "The mechanics of labriform locomotion. I. Labriform locomotion in the angelfish (*Pterphyllum eimekei*): an analysis of the power stroke," J. Exp. Biol. **82**, 255–271 (1979).

[3] R. E. Shadwick and G. V. Lauder, *Fish Biomechanics* (Academic, New York, 2006).

[4] F. E. Fish and G. V. Lauder, "Passive and active flow control by swimming fishes and mammals," Annu. Rev. Fluid Mech. **38**, 193–224 (2006).

[5] U. K. Muller, J. Smit, E. J. Stamhuis, and J. J. Videler, "How the body contributes to the wake in undulatory fish swimming flow fields of a swimming eel (Anguilla anguilla)," J. Exp. Biol. **204**(16), 2751–2762 (2001).

[6] M. J. Lighthill, "Hydromechanics of aquatic animal propulsion," Annu. Rev. Fluid Mech. **1**(1), 413–446 (1969).

[7] T. Y. Wu, "Hydromechanics of swimming propulsion. Part 1. Swimming of a two-dimensional flexible plate at variable forward speeds in an inviscid fluid," J. Fluid Mech. **46**(2), 337–355 (1971).

[8] J. A. Sparenberg, "Survey of the mathematical theory of fish locomotion," J. Eng. Math. **44**(4), 395–448 (2002).

[9] K. Singh and T. J. Pedley, "The hydrodynamics of flexible-body manoeuvres in swimming fish," Physica D: Nonlinear Phenom. **237**(14–17), 2234–2239 (2008).

[10] M. Sfakiotakis, D. M. Lane, and J. B. C. Davies, "Review of fish swimming modes for aquatic locomotion," IEEE J. Ocean. Eng. **24**(2), 237–252 (1999).

[11] M. S. Triantafyllou, G. S. Triantafyllou, and D. K. P. Yue, "Hydrodynamics of fishlike swimming," Annu. Rev. Fluid Mech. **32**, 33–53 (2000).

[12] G. V. Lauder, P. G. A. Madden, J. L. Tangorra, E. Anderson, and T. V. Baker, "Bioinspiration from fish for smart material design and function," Smart Mater. Struct. **20**, 094014 (2011).

[13] G. V. Lauder, J. Lim, R. Shelton, C. Witt, E. Anderson, and J. L. Tangorra, "Robotic models for studying undulatory locomotion in fishes," Mar. Technol. Soc. J. **45**(4), 41–55 (2011).

[14] A. Gibb, B. Jayne, and G. Lauder, "Kinematics of pectoral fin locomotion in the bluegill sunfish Lepomis Macrochirus," J. Exp. Biol. **189**(1), 133–61 (1994).

[15] E. G. Drucker and G. V. Lauder, "Locomotor function of the dorsal fin in teleost fishes: experimental analysis of wake forces in sunfish," J. Exp. Biol. **204**(17), 2943–2958 (2001).

[16] G. V. Lauder, E. J. Anderson, J. Tangorra, and P. G. Madden, "Fish biorobotics: kinematics and hydrodynamics of self-propulsion," J. Exp. Biol. **210**(16), 2767 (2007).

[17] K. A. Morgansen, B. I. Triplett, and D. J. Klein, "Geometric methods for modeling and control of free-swimming fin-actuated underwater vehicles," IEEE Trans. Robot. **23**(6), 1184–1199 (2007).

[18] N. Vandenberghe, J. Zhang, and S. Childress, "Symmetry breaking leads to forward flapping flight," J. Fluid Mech. **506**, 147–155 (2004).

[19] S. Childress, N. Vandenberghe, and J. Zhang, "Hovering of a passive body in an oscillating airflow," Phys. Fluids **18**, 117103 (2006).

[20] A. J. Bergou, S. Xu, and Z. J. Wang, "Passive wing pitch reversal in insect flight," J. Fluid Mech. **591**, 321–337 (2007).

[21] S. Alben and M. J. Shelley, "Coherent locomotion as an attracting state for a free flapping body," Proc. Natl. Acad. Sci. U.S.A. **102**(32), 11163–11166 (2005).

[22] S. Alben, "An implicit method for coupled flow-body dynamics," J. Comput. Phys. **227**(10), 4912–4933 (2008).

[23] S. E. Spagnolie and M. J. Shelley, "Shape-changing bodies in fluid: Hovering, ratcheting, and bursting," Phys. Fluids **21**, 013103 (2009).

[24] J. D. Eldredge and D. Pisani, "Passive locomotion of a simple articulated fish-like system in the wake of an obstacle," J. Fluid Mech. **607**, 279–288 (2008).

[25] E. Kanso and P. K. Newton, "Passive locomotion via normal-mode coupling in a submerged spring–mass system," J. Fluid Mech. **641**, 205–215 (2009).

[26] C. Eloy and L. Schouveiler, "Optimisation of two-dimensional undulatory swimming at high Reynolds number," Int. J. Non-Linear Mech. **46**(4), 568–576 (2011).

[27] I. Borazjani and F. Sotiropoulos, "Numerical investigation of the hydrodynamics of carangiform swimming in the transitional and inertial flow regimes," J. Exp. Biol. **211**(10), 1541 (2008).

[28] I. Borazjani and F. Sotiropoulos, "Numerical investigation of the hydrodynamics of anguilliform swimming in the transitional and inertial flow regimes," J. Exp. Biol. **212**(4), 576 (2009).

[29] S. Kern and P. Koumoutsakos, "Simulations of optimized anguilliform swimming," J. Exp. Biol. **209**(24), 4841 (2006).

[30] A. A. Shirgaonkar, O. M. Curet, N. A. Patankar, and M. A. MacIver, "The hydrodynamics of ribbon-fin propulsion during impulsive motion," J. Exp. Biol. **211**(21), 3490 (2008).

[31] M. J. McHenry, C. A. Pell, and J. H. Long, "Mechanical control of swimming speed: stiffness and axial form in undulating fish models," J. Exp. Biol. **198**(11), 2293–2305 (1995).

[32] E. G. Drucker and G. V. Lauder, "Locomotor function of the dorsal fin in rainbow trout: kinematic patterns and hydrodynamic forces," J. Exp. Biol. **208**(23), 4479–4494 (2005).

[33] G. V. Lauder and P. G. A. Madden, "Fish locomotion: kinematics and hydrodynamics of flexible foil-like fins," Exp. Fluids **43**(5), 641–653 (2007).

[34] S. Alben, "Simulating the dynamics of flexible bodies and vortex sheets," J. Comput. Phys. **228**(7), 2587–2603 (2009).

[35] S. Alben, "Optimal flexibility of a flapping appendage at high Reynolds number," J. Fluid Mech. **614**, 355–380 (2008).

[36] G. K. Batchelor, *An Introduction to Fluid Dynamics* (Cambridge University Press, Cambridge, England, 1967).

[37] M. Argentina and L. Mahadevan, Proc. Natl. Acad. Sci. U.S.A. **102**, 1829–1834 (2005).

[38] P. Saffman, *Vortex Dynamics* (Cambridge University Press, Cambridge, England, 1992).

[39] N. I. Muskhelishvili, *Singular Integral Equations: Boundary Problems of Function Theory and Their Application to Mathematical Physics* (Noordhoff, Groningen, 1953).

[40] R. Krasny, "Computation of vortex sheet roll-up in the Trefftz plane," J. Fluid Mech. **184**, 123–155 (1987).

[41] R. Krasny, "Desingularization of periodic vortex sheet roll-up," J. Comput. Phys. **65**, 292–313 (1986).

[42] M. Jones, "The separated flow of an inviscid fluid around a moving flat plate," J. Fluid Mech. **496**, 405–401 (2003).

[43] C. Eloy, C. Souilliez, and L. Schouveiler, "Flutter of a rectangular plate," J. Fluids Struct. **23**(6), 904–919 (2007).

[44] S. Alben, "Passive and active bodies in vortex-street wakes," J. Fluid Mech. **642**, 95–125 (2009).

[45] S. Alben, P. G. Madden, and G. V. Lauder, "The mechanics of active fin-shape control in ray-finned fishes," J. R. Soc. Interface **4**(13), 243–256 (2007).